Numerical Study of Mixing Enhancement in a Supersonic Round Jet

Nicolas Chauvet,* Sebastien Deck,† and Laurent Jacquin‡
ONERA, 92322 Châtillon Cedex, France

Experiments and computations are used to investigate the mixing enhancement of an underexpanded sonic jet subjected to radial secondary injections in a realistic aircraft-afterbody configuration. In accordance with more academic studies, the present study confirms that secondary jets lead to a strong distortion of the jet interface under the action of the longitudinal vortices. Reynolds-averaged Navier–Stokes computations are validated on experimental data and then used to perform a parametric study. We investigate the influence of parameters such as the number of active injectors, their aspect ratio, and the total pressure and temperature of the injected air. These computations also allow us to investigate the drastic changes in the compressible structure of the flow due to the action of the secondary injection.

Introduction

MIXING enhancement is a matter of concern for several aeronautical applications such as combustion chamber optimization, ejector-thrust augmentation, jet noise, and infrared reduction. The latter issue has motivated the present study. The jet plume of military aircraft is the primary source of aircraft infrared radiation [1–3] and so an increase in the mixing of the jet with the ambient air is sought. Because these jets operate at large Reynolds number and are usually supersonic, the problem involves turbulent mixing in the presence of shock waves and other compressibility-induced effects [4–7]. Experiments have shown that turbulent mixing in supersonic mixing layers is significantly reduced as the compressibility level is increased; they also emphasized the need for designing an efficient mixing device. An impressive research effort was developed worldwide on diverse mixing devices [8]. Nonetheless, few solutions have been proposed for conventional axisymmetric jets at supersonic regimes. Radial injections, which are studied here, are a classical means that introduce streamwise vortices to speed up the mixing rate [9–11]. Our goal is to characterize the efficiency of such a system in realistic conditions. Streamwise vortices have the advantage of being hardly influenced by the compressibility and the highly three-dimensional character [6,12,13] of the compressible mixing layers. They may also be introduced by means of corrugated or lobed trailing edges [14,15], chevrons [16,17], or solid tabs [18–21]. However, fluidic injection seems more attractive, because it can be easily adapted to the flow conditions; additionally, they are expected to reduce weight, cost, and mechanical complexity. Recent studies investigated pulsed injections in high-subsonic [17,22–25] and supersonic jets [26]. The benefit of secondary unsteadiness does not look obvious, except for reduction of injected mass flow [11,27]. The present work focus on steady injection. Davis [9] considered two oppositely oriented radial jets. He observed that a low-momentum injection increases the mixing-layer growth rate, whereas a high-momentum injection leads to a more dramatic distortion of the jet mean interface. Collin et al.

[11] focused on the interaction of the primary-jet mixing layer and the radial secondary jet in a fully expanded jet regime and observed an intrinsic unsteady nature of this interaction. Following these authors, this unsteadiness could be a possible source of the shear-layer growth-rate enhancement. However, they also found that this effect is only local, the standard spreading being recovered in the far field. The same was observed in a purely incompressible jet-mixing-layer interaction [28]. Also note the interesting concepts based on destabilization of the mixing layer by means of parallel coflows [29] or counterflows [30].

The present study was conducted in the framework of a research program on alleviation of the infrared signature of propulsive jets. An experiment was conducted in the S3Ch transonic wind tunnel at ONERA. The experiments were for evaluating the influence of the nozzle pressure ratio (NPR) and the number of secondary injectors and their flow rate. This parametric study was completed by means of Reynolds-averaged Navier–Stokes (RANS) computations. These simulations also allowed us to scrutinize several aspects of the flow that cannot be described by way of experimental methods. Literature shows that secondary injections are efficient both in subsonic and supersonic jet regimes [20], indicating that mixing enhancement is primarily due to vortex induction. In the supersonic jet, compressibility effects occur through changes in the expansion conditions of the jet in the presence of the secondary jets. We investigate how the wave patterns are modified by the control devices and how this participates in the changes of the jet-mixing properties. Mixing criteria are proposed to quantify the efficiency of the fluidic system. On the whole, our study provides a parametric investigation highlighting important elements that must be taken into account to design efficient mixing systems.

Experimental Setup

Experiments were carried out in the S3Ch continuous research wind tunnel of ONERA's Chalais Meudon center. The test section is square-shaped and the dimensions of the test chamber are 0.78×0.78 m^2. The apparatus (see Fig. 1a) is based on a representative combat-aircraft afterbody delivering a primary sonic jet surrounded by an annular secondary flow ventilation. It is mounted on a profiled sting. A sketch of the model and a close-up of the fluidic control system is given, respectively, in Figs. 1b and 1c. The far-field conditions of the external stream are $M_0 = 0.8$ for the Mach number, $p_0 = 0.66 \cdot 10^5$ Pa for the static pressure, and $T_{i0} = 300$ K for the total temperature. The primary jet is completely characterized by its stagnation conditions $T_{i1} = 300$ K and $p_{i1} =$ NPR $\times p_0$. Two nozzle pressure ratios were tested corresponding, respectively, to the cruise regime (NPR = 3.1) and to the full-throttle regime (NPR = 5.0). The ventilation stream is determined by its total

*Ph.D. Student, Applied Aerodynamics Department, 29 Avenue de la Division Leclerc.

†Research Engineer, Applied Aerodynamics Department, 29 Avenue de la Division Leclerc; sebastien.deck@onera.fr (Corresponding Author).

‡Head, Fundamental and Experimental Aerodynamics Department, 29 Avenue de la Division Leclerc.
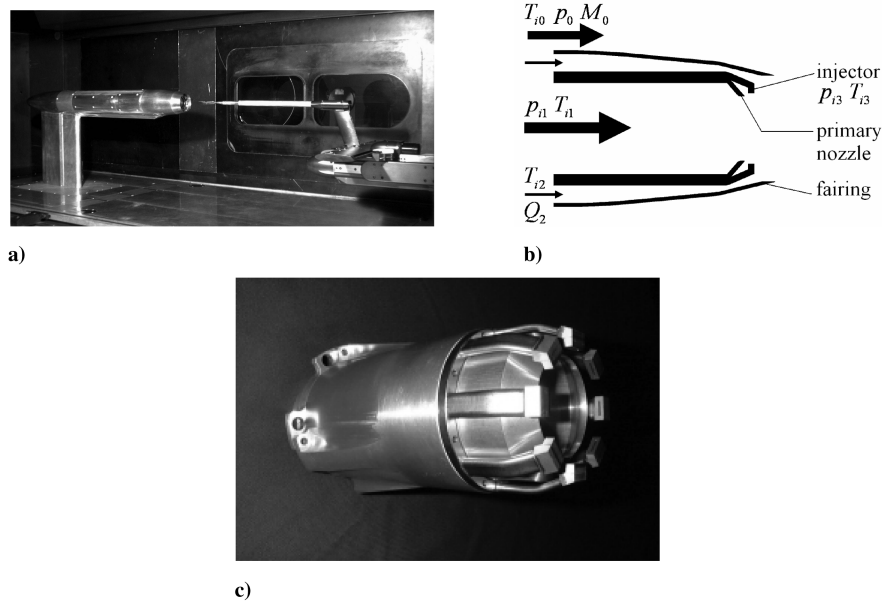
Fig. 1 Experimental setup: a) overview of the afterbody model in the transonic wind tunnel test section, b) sketch of the afterbody, c) close-up on the fluidic control system around the primary-jet exit section.

temperature $T_{i2} = 270$ K and its mass flow rate from $Q_2 = 22$ to 34 g/s. Several fluidic control devices were tested. They consist of eight radial injectors (see Fig. 1c). An arbitrary number of these injectors can be activated. The injected air is cold ($T_{i3} = 300$ K) and the mass flow rate was varied from $Q_3 = 14$ to 42 g/s. The flowfield was characterized by means of schlieren visualizations, tomoscopic pictures, pressure and temperature measurements, and two-component particle image velocimetry (PIV). A complete description of the experiment is available in [31].

Simulation Overview

Numerical investigations were performed with FLU3M code developed by ONERA. It solves the Navier–Stokes equations on multiblock structured grids. The Navier–Stokes equations are discretized using a second-order finite volume scheme on a cell-centered stencil. Roe's flux difference splitting is employed for the advective fluxes, and the MUSCL approach extends the spatial accuracy to the second order. Harten's correction with a coefficient equal to 10^{-4} is employed to avoid a wrong behavior of entropy. All viscous terms are centrally differenced. Time integration is based on second-order-accurate Gear's formulation [32,33], and the inversion of the implicit system is performed by means of a LU-SGS factorization. Owing to the approximations done in the implicit stage, Pulliam's inner iteration algorithm was implemented to restitute the time accuracy. More details concerning the numerical method and implementation of turbulence models can be found in [33,34]. This well-tried solver was notably used to compute a large eddy simulation (LES) of the flow over a cavity at high Reynolds number [35], zonal-detached-eddy simulations (ZDES) of transonic buffet over a supercritical airfoil [36] and the flow around a high-lift configuration [37], several hybrid RANS/LES of supersonic base flows [38], and LES of a synthetic jet in a crossflow [39].

In the present work, investigation of various configurations was made by using RANS simulations with the Spalart–Allmaras turbulence model [40,41]. This model is widely used in complex compressible flow situations. Georgiadis et al. [42] performed computations on a lobed nozzle with several linear and nonlinear turbulence models and concluded that the Spalart–Allmaras model provided solutions in reasonable agreement with experimentally measured velocities. Payne et al. [43] compared this model to other popular models, a low Reynolds number $k - \epsilon$ model and the Wilcox $k - \omega$ model, on a supersonic jet in a transonic crossflow; the Spalart–Allmaras model showed fair agreement with both the downstream total pressure and vorticity data. Because the
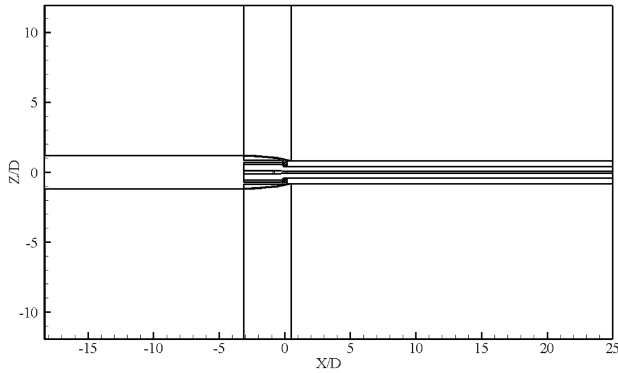
streamwise vorticity plays a role in the flows considered here, a rotation correction proposed by Dacles-Mariani et al. [44] was used to limit excessive turbulent diffusion in the vortex cores.

All of the computed configurations are gathered in Table 1. In this table, $\Lambda = R\Delta\theta/\Delta x$ denotes the aspect ratio of each injection orifice, where Δx and $R\Delta\theta$ are, respectively, the streamwise and spanwise lengths. The basic geometries of the experimental test cases were reproduced. Additional cases corresponding to different injector geometries were also simulated. Preliminary numerical tests not presented in this paper indicated some crucial points that have to be taken into account. They emphasized, in particular, the sensitivity of the jet structure to the external boundary-layer thickness. This explains why the boundary layer is calculated along a cylindrical wall representative of the sting. Furthermore, they showed that it is necessary to carry out 3-D simulations on the whole jet to properly capture the shock reflection pattern. Five different meshes of approximately eight million cells were created for the two- and four-active-injector configurations. The computational field extends over $12D$ (D being the throat diameter) in the radial direction and over $18D$ upstream and $25D$ downstream of the nozzle throat, respectively. However, the finest mesh covers only the maximum area probed during the experiment (i.e., $9D$ downstream of the nozzle). There are 304 cells in the jet direction and 128 cells in the azimuthal direction. To capture the streamwise vortices, the cells are clustered near the operating injectors and homogeneously distributed in the jet. The mesh corresponding to cases 1–3 and 9–13 is displayed
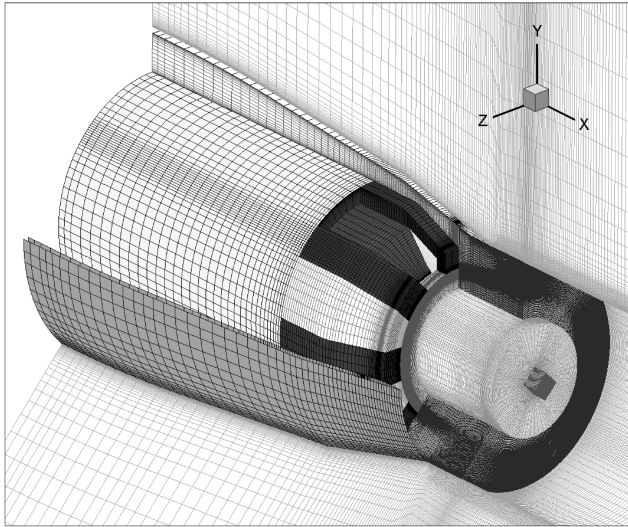
Table 1 Characteristics of the 13 computed configurations (experimental cases are also indicated by "exp")

Case no.	NPR	T_{i1}, K	N	Λ	Q_3, g/s	p_{i3}/p_{i1}	T_{i3}, K
1(exp)	3.1	300	0	——	——	——	——
2(exp)	3.1	300	4	10	14	1.42	300
3(exp)	3.1	300	4	10	26	2.79	300
4(exp)	3.1	300	8	10	26	1.39	300
5	3.1	300	2	10	26	5.57	300
6	3.1	300	4	2.5	26	2.79	300
7	3.1	300	4	1	26	2.79	300
8	3.1	300	4	0.5	26	2.79	300
9	3.1	300	4	10	18	2.79	600
10	3.1	300	4	10	13	2.79	1200
11	3.1	1100	0	——	——	——	——
12	3.1	1100	4	10	26	2.79	300
13	3.1	1100	4	10	13	2.79	1100

in Fig. 2. Another mesh of about 10.5 million cells was built for the eight-active-injector case. It is made of 168 cells in the azimuthal direction. The latter mesh enabled us to verify grid convergence. For instance, the axial pressures computed in cases 1 and 3 on both grids are displayed in Fig. 3. The behavior of the axial pressures will be fully discussed in the following sections. The stagnation conditions p_{i1} and T_{i1} are imposed at the inlet boundary of the primary nozzle, whereas the mass flow rate Q_2 is set at the entrance of the ventilation duct, together with the stagnation temperature T_{i2}. Each injector-exhaust flow is explicitly calculated in small convergent nozzles with flat parallel throats to provide uniform flows. The external-flow boundaries are based on Riemann-characteristic invariants for subsonic flows, and the jet exit has a nonreflective supersonic condition.

The cases investigated experimentally are also indicated in Table 1 by "(exp)." A comparison between numerical and experimental results is made on cases 1 to 3 in the following sections. Different parameters of the control were varied to judge their efficiency in the mixing enhancement. In this way, cases 3, 4, and 5 were used to assess the influence of the injector number N; cases 3, 6, 7, and 8 assessed the aspect ratio $\Lambda = R\Delta\theta/\Delta x$ of the injector orifices; cases 2 and 3 assessed the control-jet pressure p_{i3}; and cases 3, 9, and 10 assessed the control-jet temperature T_{i3}. Because all of the previous tests concerned cold jets, additional cases 11, 12, and 13 were created to estimate the mean temperature reduction induced by several injection configurations. Because the goal of these latter tests was to numerically investigate the influence of temperature, the specific heat capacities ratio $\gamma = 1.4$ was not changed.

Flowfield Induced by the Four-Injector Control Device
External Shape of the Jet

An overall view of the changes in the jet due to the fluidic control device is displayed in Fig. 4. The figure depicts the surface of constant Mach number $M = 1$, which approximately gives an idea of the jet boundary. In the reference jet (on the bottom of Fig. 4), one can notice that the quasi-axisymmetric shape of the jet exhibits pinches and bulges corresponding to the reflections of compression and expansion waves. When the control is activated (on the top of Fig. 4), a dramatic distortion of this surface is obtained under the action of the injected momentum in the near field of the radial injections. This action is also persistent further downstream because of the streamwise vortices that are characteristic of the transverse injection far field [45,46].

The streamwise vorticity ω_x, nondimensionalized by $2a^*/D$ (where a^* is the sound velocity at the throat and D the diameter), $\Omega_x = \omega_x/(2a^*/D)$, is displayed at the top of Fig. 5 in several cross sections, together with the lines of constant $p_i/p_{i0} = 1.05$. Injectors are blowing in the horizontal and vertical directions. This figure highlights the vortex induction mechanism previously described by Zaman [47,48]. The scenario is as follows. A counter-rotating vortex pair (CVP) is generated by each secondary jet [45,46] and then moves to the main jet axis under its own induced velocity [see the arrows in Fig. 5 ($X/D = 0.5$)]. When the CVP are sufficiently close to each other, their mutually induced velocity becomes strong enough to separate the initial vortex couples and to form new couples that move away in the median initial directions [the diagonal arrows

a)

b)

Fig. 2   Computation grid: a) large view and b) details around the afterbody.

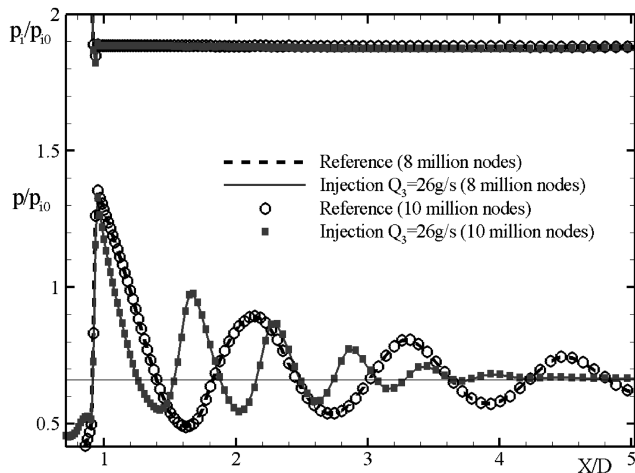**Fig. 3   Static pressures and total pressures on the axis of the reference jet and the controlled jet, for 8 and 10.5 million nodes.**
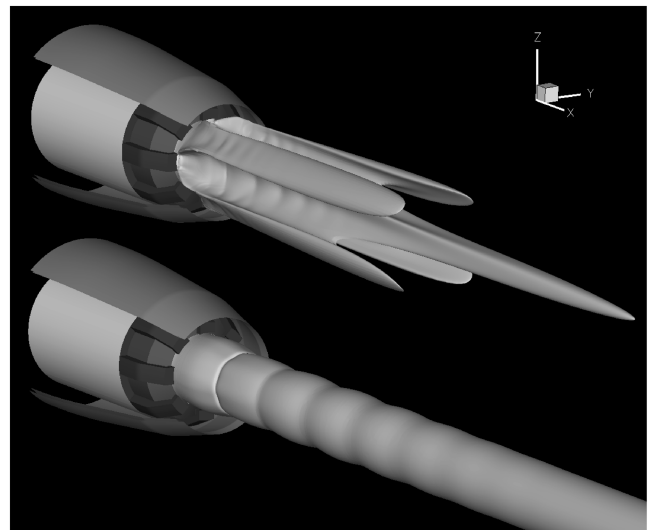
Fig. 4   Effect of four radial injections on the jet contour (surface Mach is 1); reference jet on the bottom side and controlled jet on the upper side.
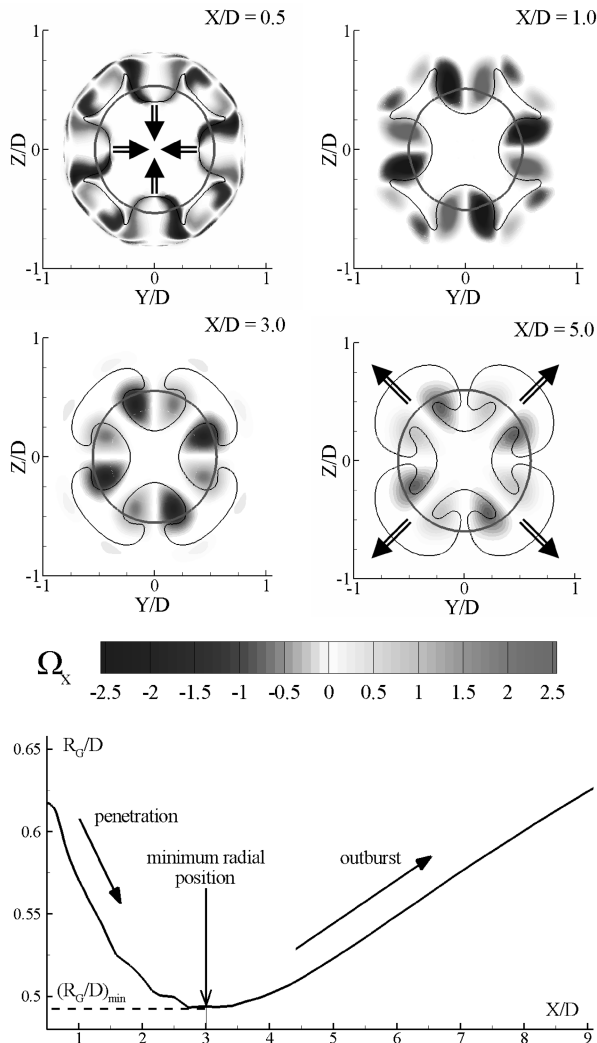
Fig. 5 Streamwise evolution of the longitudinal vortices; top: vorticity contours in the jet controlled by four active injectors (case 3), $p_i/p_{i0} = 1.05$ is the controlled jet (thin line), $p_i/p_{i0} = 1.05$ is the uncontrolled jet (thick circular line); bottom: radial position of the vortices R_G/D along the jet axis.

in Fig. 5 ($X/D = 5.0$)]. This motion can be illustrated by plotting the streamwise evolution of the radial position of the longitudinal vortices. Owing to the symmetry of the injection, all of the vortices have the same radial position at each longitudinal location X. Hence, this radial position can be defined by the barycenter of vorticity:

$$R_G(X) = \frac{\int_0^{2\pi/(2N)} \int_0^{R_\infty} \omega_x^+(X, r, \theta) r^2 \, dr \, d\theta}{\int_0^{2\pi/(2N)} \int_0^{R_\infty} \omega_x^+(X, r, \theta) r \, dr \, d\theta} \qquad (1)$$

with $N = 4$ injectors and where R_∞ and $\omega_x^+(X, r, \theta)$ denote, respectively, the radius of the computational domain and the local positive vorticity field in the streamwise direction X [$\omega_x^+ = (\omega_x + |\omega_x|)/2$]. This radial position R_G, nondimensionalized by the throat diameter D, is plotted on the bottom of Fig. 5. One can clearly identify two stages: first, the penetration symbolized by converging arrows in the cross section ($X/D = 0.5$) of Fig. 5, and second, the outburst symbolized by diverging arrows in the cross section ($X/D = 5.0$).

Internal Structure of the Jet

Figures 6a and 6b show, respectively, schlieren visualizations of both experiment and computation of the NPR = 3.1 reference jet. It exhibits a transonic compression lens that is characteristic of weakly underexpanded sonic jets, that is, for which the NPR is barely above the critical NPR* necessary to reach sonic conditions (NPR* = 1.89

if $\gamma = 1.4$). While increasing the plenum pressure, this compression wave lens forms before the Mach disk, which occurs at higher NPR [49]. This shock occurring very near the full-expansion regime was already observed in former experiments [50], but, to the authors' knowledge, no distinction has ever been made in literature with the classical Mach disk. Figures 6c and 6d illustrate the effect of the secondary injections on the propagation of the compression waves within the jet. The section of Fig. 6d extracted from the computations cuts the plane of two active injectors. The resulting shock wave pattern seems to be similar to a Mach disk. Looking for an explanation of the Mach disk occurrence, it may be inferred that the shocks formed ahead of the injections play the role of the incident shock and are then responsible for the new shock pattern. Two arguments show that it cannot be possible. If it were the case, each bow shock, becoming a compression evanescent wave when propagating downstream, would reflect as an expansion wave, if we consider that the jet boundary is isobaric. The reflected wave cannot then give rise to a coalescence shock necessary to the onset of the Mach disk. More evidence that invalidates the assumption is emphasized in the controlled jet with a higher nozzle pressure ratio, NPR = 5, presented in [49]. Figure 7 represents the Mach/shock waves extracted from the computation of this jet, together with the reference jet at NPR = 5.0. In the reference jet, one can notice that the compression waves coalesce in an oblique shock and eventually form a Mach disk, typical of high-NPR jets [50]. The controlled jet (NPR = 5) has a very similar wave structure to that of the mildly underexpanded jet (NPR = 3.1) presented herein, although the wave slopes are steeper. One can notice that the compression waves, reaching the edges of the Mach disk (the triple point in the plane flow, point 3 in Fig. 7b) are originating from points of the jet boundary (point 2 in Fig. 7b), which are located ahead of the region in which the evanescent bow shock impacts the jet boundary (point 1 in Fig. 7b). A deeper investigation based on the analysis of Mach waves reveals that transverse mass flows due to the bypass of the secondary jets are responsible for the previously described wave behavior, together with the modification of the pressure gradients along the jet boundary. This analysis, which is beyond the scope of this study, is thoroughly described in [51].

Figure 8 shows the Mach number field in the longitudinal section of the reference jet (quasi axisymmetric), and in two different planes of the controlled jet. One plane crosses the operating injectors and is called the *injection plane* (middle picture), whereas the other plane is located between two adjacent active injectors and is called the *interplane* (bottom picture). The strong jet constriction in the injection planes in contrast to the large jet expansion in the interplanes allows us to understand the discrepancies noticed in Fig. 6. The jet distortion capability was also seen to hold at higher NPR regimes [49].

To improve mixing by an action on the mean shock structure, the control device would have to increase the vorticity inside the jet by generating shock intersections. Figure 8 indicates that the wave structure modified by radial injections does not induce a significant change in shock interactions. Similar results were noticed in a higher underexpansion jet regime (NPR = 5) [49]. It can then be concluded that the change in the mean shock structure resulting from the secondary-jet activation cannot significantly improve the jet mixing. Therefore, as claimed by Zaman et al. [20] for a jet perturbed by tabs, the only significant mean flow mechanism responsible for the mixing enhancement is the longitudinal vortex dynamics.

Axial Pressures

It is worth noting the axial total and static pressure signature of the controlled jet (see Fig. 9a). One can notice that the location of the strong shock at location $X/D \approx 0.95$ and the pressure oscillations that are characteristic of the compression/expansion cells. In addition, the experiment reveals the conservation of the static pressure amplitudes and of the total pressure in the reference case. Activation of the secondary jets then produces a reduction in the static pressure period and a decrease of the total pressure. The latter change proves that turbulence has reached the jet axis region. The
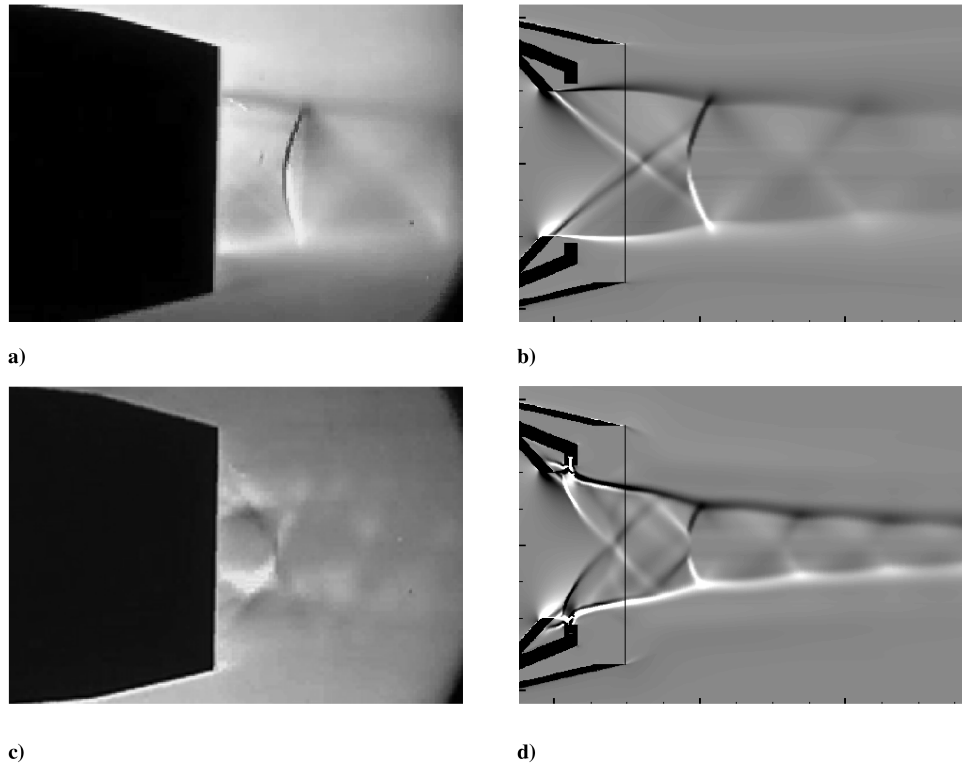
Fig. 6   Schlieren visualizations of the uncontrolled jet (top) and controlled jet (bottom): experiment (left) and numerical results (right).
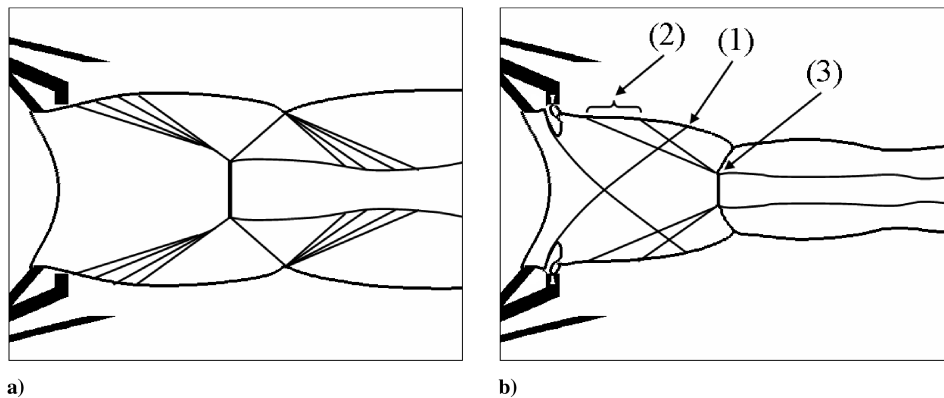

Fig. 7   Scheme of the Mach/shock waves in a) the reference jet and b) the controlled jet (injection plane) for NPR = 5.0.

effect of the injected mass flow rate is displayed in Fig. 9b and shows that the higher the mass flow rate, the lower the period and the more amplified the attenuation of the static pressure picks. The CFD results are in qualitative accordance with the static pressure evolution, but they do not reproduce the total pressure behavior. This is due to longer potential cores, namely, of $9.1D$ for the reference jet and $5.0D$ for the controlled jet. These discrepancies indicate that the Spalart–Allmaras model does not correctly reproduce all of the features of the compressible shear layer studied here. Nevertheless, a fair agreement on the velocity field is found with PIV results (see Fig. 9c). Corroborating the damping of the pressure oscillation, one can see that compression/expansion cells of the reference jet are attenuated by RANS calculation.

As shown by all of the results described previously, the mixing process in this flow is a complex one. The intrinsic three-dimensional nature of the controlled jets has to be taken into account to assess the actual mixing capability of a hyper-mixing device.

Mixing Enhancement Criteria

Beforehand, the notion of mixing must be described in terms of physical mechanisms and then quantified by physical variables. In

this paper, mixing designates all of the processes that increase the exchanges between several fluids of different characteristics in such a way that any heterogeneous flow is brought to a uniform flow. Among these mixing processes, one can distinguish molecular and turbulent mechanisms. At the large scale of the averaged fluid motion, turbulent mixing is approximated to a turbulent diffusion process. The present study adopts this observation level, because it is based on RANS simulations.

To evaluate the mixing rate, one can consider either variables giving some information of the turbulence activity or variables characterizing the result of the mixing process. Because turbulence is modeled in this study, we adopt the second choice. Thus, the following criteria will have to quantify the level of homogenization reached by the tested controlled jets under the action of both molecular and turbulent mechanisms, but will not be able to distinguish between one and the other.

If we consider the mixing of chemical species with no chemical reaction, mass conservation states that the mass of each chemical component in a given material domain is constant in time. Therefore, the mixing of different species solely manifests itself in a diffusion process. The use of a passive scalar is then the most appropriate way to evaluate mixing. Nonetheless, because the jets studied herein are
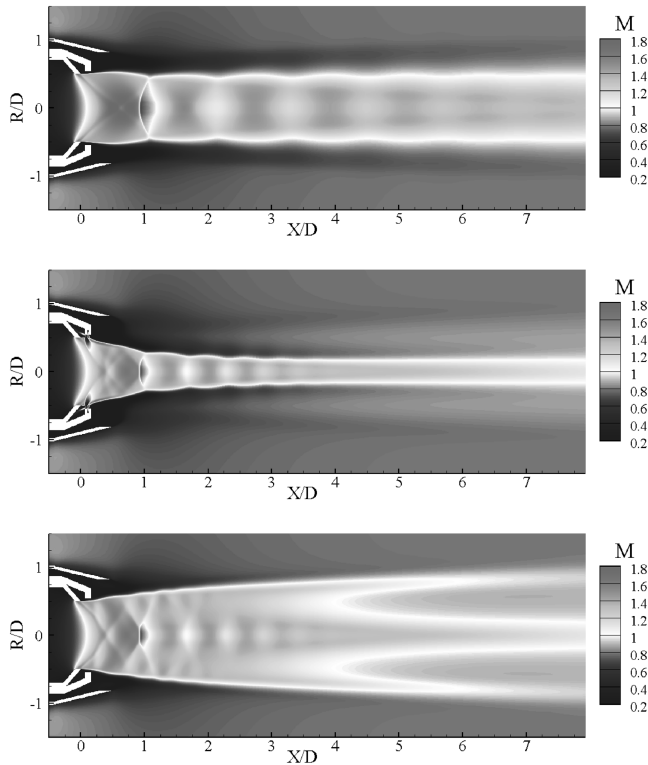
Fig. 8 Comparison of the Mach number contours (simulations NPR = 3.1); reference jet in the upper side and controlled jet in the middle and in the bottom side.

made of the same molecules as the surrounding air, and in absence of a passive scalar, the mixing criteria used in this study will be based on the local fluid state.

The local fluid state on which a criterion can be defined must be invariable when mixing is inactive and must be sensitive to mixing

activity. Out of any mixing process (i.e., in a perfect flow with neither viscosity nor thermal conductivity and without any shock losses), the isentropic pressure p_i and the isentropic temperature T_i are conserved along the fluid motion, provided that no shock occurs (for p_i). On the other hand, molecular mixing related to viscous friction and heat conduction modifies the evolution of p_i and T_i. In addition, turbulent mixing increases the diffusion of both quantities. The stagnation conditions p_i and T_i then seem to be appropriate to quantify mixing. However, and contrary to a passive scalar or to the stagnation temperature, the stagnation pressure is not only subjected to diffusion but is also altered by dissipation, both phenomena being intricately linked.

Besides, jet flows are basically higher-p_i regions, whereas their T_i level can be equal to that of the external fluid. This is the case of the cold jets studied herein. This fact explains why a first series of criteria are proposed on the stagnation pressure field only. They may be applied to cold jets as well as to hot jets. Stagnation pressure is also sensitive to shocks, whereas stagnation temperature is not. As far as the mean flow is concerned, shock phenomenon is distinct from mixing, and so if the shocks are strong enough, any criterion based on p_i is not reliable. Therefore, we can conjecture that criteria based on T_i in place of p_i would likely be more appropriate for the estimation of the mixing of highly underexpanded hot jets in which the shock influence might become significant. Fortunately, we have previously seen that weak shocks do not significantly alter the total pressure in our cases, which justifies the use of stagnation pressure to assess the mixing in the present study. Moreover, this choice is dictated by experiments that very easily give access to total pressure.

Both local and global mixing criteria are now defined to highlight different aspects of the influence of the control on the jet flow. These criteria will be used in the next section to evaluate the mixing efficiency of several control variations.

Local Mixing Criteria

An equivalent jet diameter D_{eq} is first defined by integrating the cross-sectional area A in which the stagnation pressure is slightly larger than the ambient total pressure. A value of $p_{iext} = (0.95p_{i0} +$
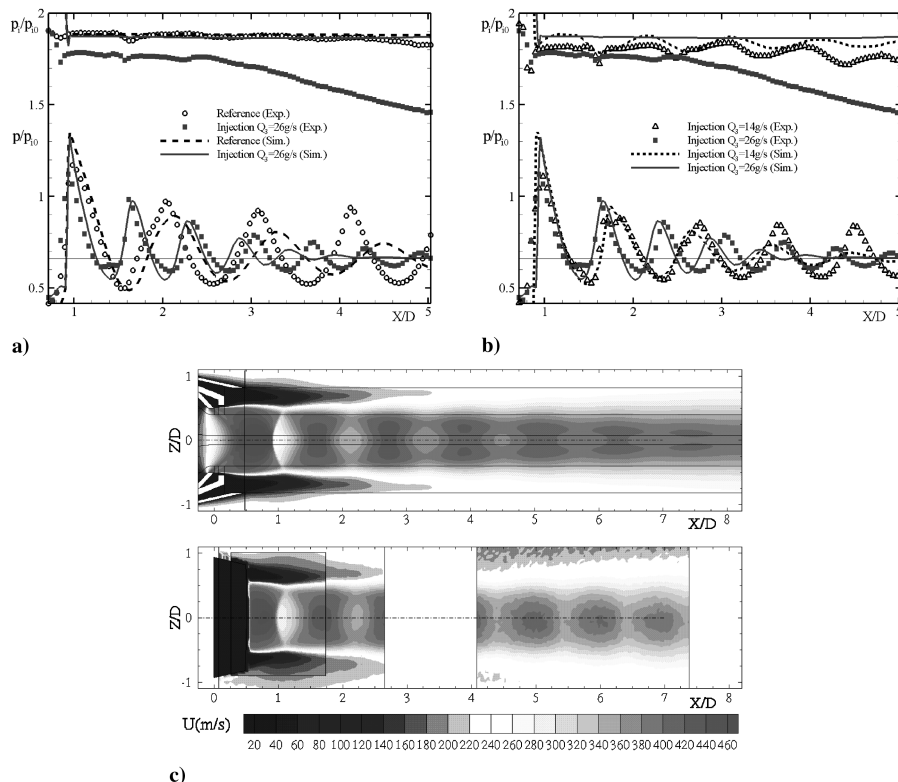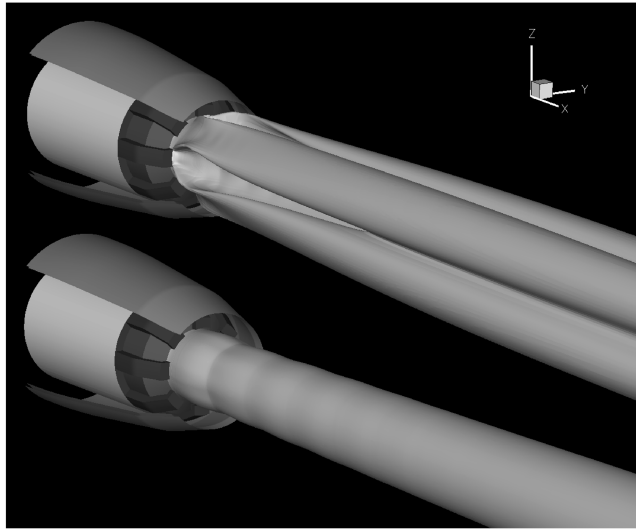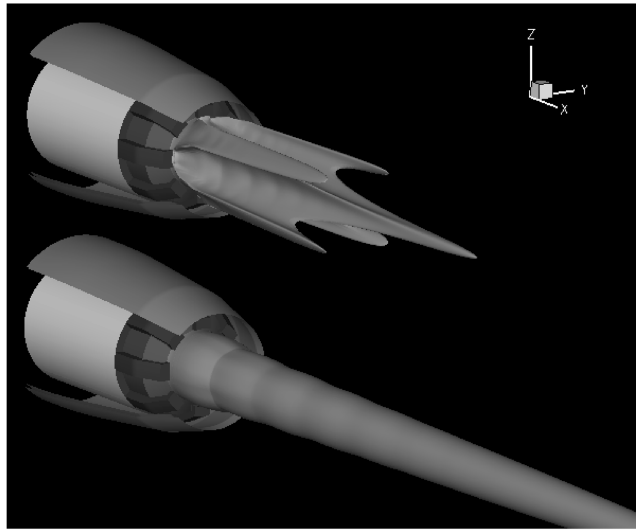

Fig. 9 Comparison numerical field vs measurements: a) effect of the control on axial static pressure and total pressure; b) effect of the control mass flow rate on axial static pressure and total pressure; and c) axial velocity field of the reference jet resulting from computations (top), 2-D/2C-PIV (bottom).
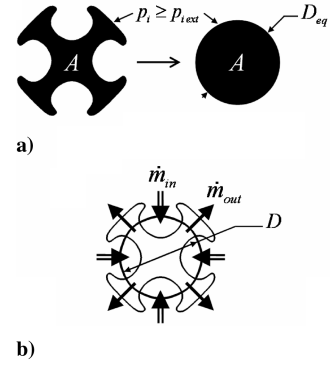
a)

b)

Fig. 10   Effect of four radial injections on the a) external jet surface (iso-$p_i = p_{i\text{ext}}$) and b) core surface (iso-$p_i = p_{i\text{core}}$); reference jet in the bottom side, controlled jet in the upper side.

a)

b)

Fig. 11   Illustration of the local criteria definition: a) equivalent diameter D_{eq} and b) incoming mass flow $\dot{m}_{\text{in}}$ and outgoing mass flow $\dot{m}_{\text{out}}$.

$0.05 p_{i1}$) is chosen. Figure 10a illustrates the surface of constant $p_i = p_{i\text{ext}}$, and Fig. 5 shows the contours enclosing the cross-sectional area A in cases of both control off and control on with four active injectors. D_{eq} can be interpreted as the diameter of an equivalent disk of the same area: $D_{\text{eq}} = \sqrt{4A/\pi}$ (see Fig. 11a). This equivalent jet diameter gives an estimation of the high jet momentum spreading. The expansion of the equivalent jet diameter is represented for various injection geometries in Figs. 12a and 12b.

By integrating the averaged stagnation pressure $\langle p_i/p_{i0} \rangle$ on the cross sections defined previously, one can assess the dilution of the jet kinetic energy with the surrounding slower stream. Figures 12c and 12d show the evolution of this quantity along the jet axis. When the mixing process is achieved, $\langle p_i/p_{i0} \rangle$ tends to unity, because the finite initial jet area spreads into an unbounded $\langle p_i/p_{i0} \rangle = 1$ volume. The closer $\langle p_i/p_{i0} \rangle$ reaches unity, the faster the homogenization caused by mixing.

To evaluate the macroscopic crossflow entrainment, which is caused by both the velocity field induced by the longitudinal vortices and by the turbulent entrainment, we consider a cylinder for which the contour is defined by the circle of the nozzle throat (of diameter D) and the axis is that of the jet. Integrating the incoming cross mass flow rate $\rho u_r < 0$ on the circular contour at each longitudinal position, we get a value for the outer fluid mass injected into the jet per second and per unit longitudinal length of $-\dot{m}_{\text{in}} < 0$ (see

Fig. 11b). In the same way, integrating the outgoing cross mass flow rate $\rho u_r > 0$, we get a value for the jet flow ejected toward the ambient air of $\dot{m}_{\text{out}} > 0$. These quantities, divided by the jet exit mass flow, are represented in Figs. 12e and 12f. For the reference jet, because the flow is axisymmetric, either the ingoing or the outgoing cross mass flow is zero, which is not the case for any of the controlled jets. Contrary to previous criteria, the latter two criteria are relative to the conditions preliminary to mixing. Indeed, macroscopic (with regard to the turbulence scales) in and out fluid motions induced by the longitudinal vortices stretch the transfer area and support the flow gradients. Thus, macroscopic crossflows seem to be an essential feature to improve. Moreover, in the RANS method presently used, we are more confident in the explicit simulation of the macroscopic convection than in the capability of the turbulence model to reproduce all of the fine turbulent mechanisms. This supports the use of a criterion based on the macroscopic flow transfers, even if it is known that the wake vortex dynamics are influenced by turbulent entrainment [52–54].

Global Mixing Criteria

The previously defined criteria are local to a cross section of the jet and permit one to draw the progression of the mixing process along the jet axis. To have single-value criteria, we give some global figures that are representative of the mixing enhancement of the whole jet volume.

Table 2 provides these quantities, integrated in the range of $x/D = 0$. to 9.6. In this longitudinal range, the *jet volume* is defined as the volume of the fluid such as $p_i \geq p_{i\text{ext}} = (0.95 p_{i0} + 0.05 p_{i1})$, where p_{i0} and p_{i1} are, respectively, the external stagnation pressure and the initial stagnation pressure of the jet. It is the volume surrounded by the surface, depicted in Fig. 10a. This criterion globally represents the jet expansion, as D_{eq} does locally.

The area of the external surface of the jet volume, namely, the surface for which the points are such that $p_i = p_{i\text{ext}} = (0.95 p_{i0} + 0.05 p_{i1})$, is referred to as the *jet area* in Table 2. It is the area of the surface shown in Fig. 10a. All of the tabulated values are related to the reference jet area. The jet surface designates the approximate spatial location at which the shear layer begins to transfer momentum from the jet flow to the external flow.

To assess the boundary shape distortion, one must first deduce a mean jet section area A and a mean contour length L by, respectively, dividing the jet volume and the jet area by the integration distance $9.6D$. Second, one must define a *shape factor* $SF = L^2/(4\pi A)$. Its minimum value of $SF = 1$ is reached for a circular jet section. The more distorted the jet contour, the larger the shape factor.

Table 2 also gives the averaged stagnation pressure in the jet volume. It is worth noting that all of the quantities written in this table are nondimensionalized by the corresponding quantities of the reference jet. This provides an integral estimate of the diffusion capability of each controlled jet.

Because shocks occur inside the jet, it is impossible to characterize the potential core volume by a domain in which $p_i \geq (0.95 p_{i1} +$
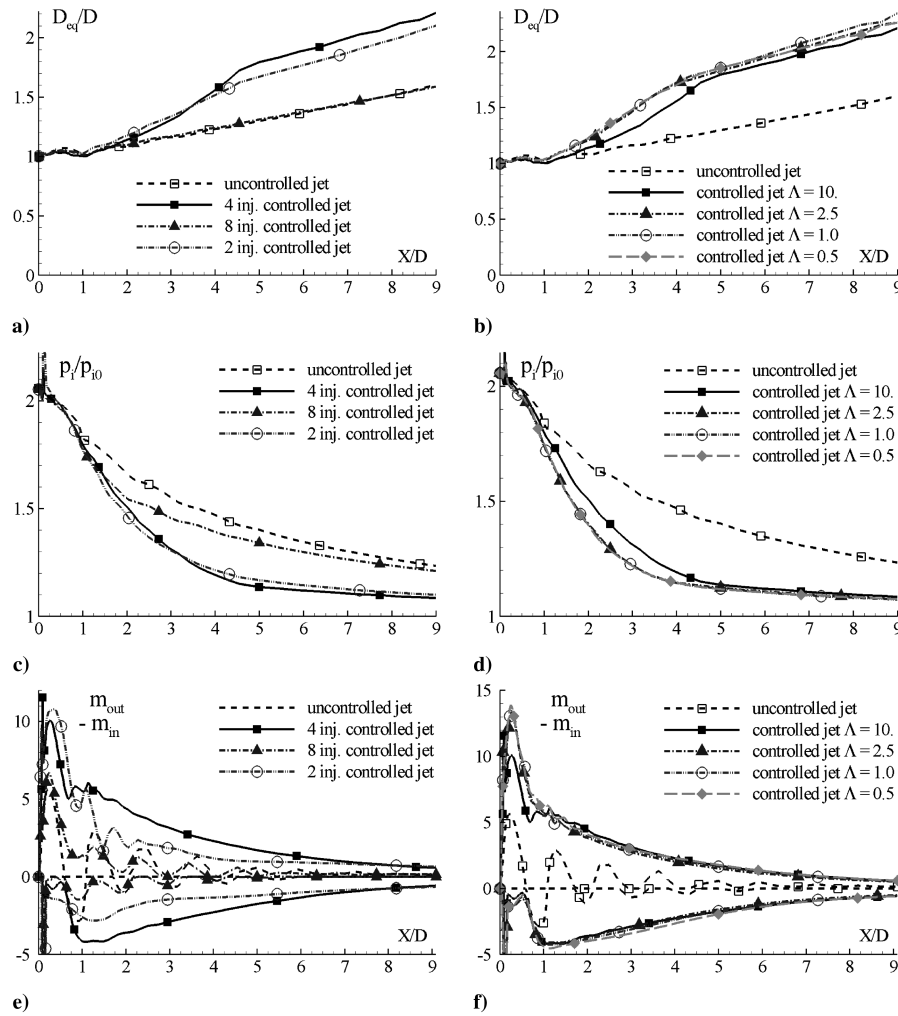
Fig. 12   Effect of various parameters of the control device.

$0.05 p_{i0}$), which would be the counterpart of the jet volume defined earlier, as would be appropriate for a subsonic jet. As a substitute, one can look at a core volume defined as $p_i \geq p_{i core} = 0.5(p_{i1} + p_{i0})$, which roughly extends to the inner half of the mixing layer. This core volume, represented in Fig. 10b, stands for the spatial extension of the high mechanical energy of the jet. A mixing device should diffuse and dissipate the initial kinetic energy of the jet and then lower the core volume as much as possible.

Table 2 also indicates the value of the ingoing and outgoing cross mass flows per unit length defined previously, integrated in the field $x/D = 0.$ to 9.6 (respectively, $\dot{M}_{in}$ and $\dot{M}_{out}$). The values written in Table 2 were subtracted by the cross mass flow of the reference jet and then nondimensionalized by the jet exit mass flow.

The following considerations sum up the objectives of the control device in terms of the global mixing criteria. With reference to the uncontrolled jet, the mixing device will have to lower the spatial

extension of the high mechanical energy, namely, minimize the core volume, while accelerating the diffusion of high mechanical energy, that is, increasing the jet volume and decreasing the mean stagnation pressure. This will be achieved by expanding the turbulent transfers with a greater jet area and amplified macroscopic crossflows. In addition, the shape factor characterizing the spreading of the exchange area with respect to the volume to dilute has to be as great as possible.

Additional Criteria

For hot jets, an estimation of the effect of the control on the temperature field is given by the quantity $\tau = T^4 - T_0^4$, integrated on the whole exterior volume visible from the lateral side of the afterbody. T_0 is the far-field exterior static temperature, and the exponent comes from the radiative application (Stefan's law). We

Table 2   Global mixing enhancement criteria (nondimensionalized quantities, the reference cases being no. 1 for cold jets and no. 11 for hot jets)

Case no.	1	2	3	4	5	6	7	8	9	10	11	12	13
x_c/D	1	0.73	0.54	0.95	0.14	0.43	0.45	0.43	0.56	0.56	1.	0.63	0.63
Core volume	1	0.73	0.49	0.80	0.45	0.40	0.40	0.39	0.48	0.49	1	0.51	0.51
Jet volume	1	1.21	1.63	0.92	1.50	1.78	1.83	1.80	1.63	1.62	1	1.30	1.28
Jet area	1	1.49	2.31	1.21	1.75	2.26	2.37	2.35	2.34	2.41	1	2.13	2.07
Shape factor	1	1.81	3.23	1.56	2.02	2.85	3.02	3.04	3.32	3.54	1	3.46	3.31
Mean P_i	1	0.91	0.82	0.96	0.84	0.80	0.79	0.79	0.82	0.82	1	0.85	0.85
$\dot{M}_{in}$	0	0.23	1.00	0.10	0.66	0.97	1.04	1.11	0.97	0.96	0	0.56	0.50
$\dot{M}_{out}$	0	0.30	1.15	0.13	0.81	1.13	1.19	1.26	1.13	1.13	0	0.60	0.54
ΔT, %	——	——	——	——	——	——	——	——	——	——	0	−1.8	12.3
TL, %	0	0.22	3.05	0.66	1.87	3.20	3.33	3.59	2.96	2.75	0	2.17	2.30

define the quantity $\Delta T = [\tau - \tau(\text{ref})]/\tau(\text{ref})$, where τ is calculated in the jet under consideration and $\tau(\text{ref})$ is the reference hot jet value (case 11). If $\Delta T < 0$, the variation in the jet temperature will contribute to lower the thermal signature. For cold jets, ΔT is meaningless, because the jet static temperature is smaller than the external temperature and so it was not computed.

Finally, the net thrusts F_T were computed by integrating $\rho u^2 + p - p_0$ on the exit surface of the afterbody. The thrust loss is then defined by $\text{TL} = [F_T(\text{ref}) - F_T]/F_T(\text{ref})$. Variations in the external pressure applied on the fairing were shown to bring a negligible contribution to the thrust loss. The thrust losses TL are displayed at the end of Table 2.

Parametric Study of the Injection System

Discussion on the Control Parameters

Before performing the parametric study, we determine the number of significant parameters controlling the system under investigation according to given assumptions. Here, the primary-jet conditions are kept constant, and we postulate that the predominant action of the radial injections is performed by means of the momentum. Thus, in a first order of approximation, the blowing condition of each injector is described by three independent state variables (for example, primary variables at the injector exit: ρ_3, V_3, and p_3) and two geometric variables (for example, the streamwise opening thickness Δx and the spanwise dimension of each hole $R\Delta\theta$). The choice of these parameters is arbitrary. We chose to successively take two state variables to characterize the stagnation conditions p_{i3} and T_{i3}, one state variable (the Mach number M_3) to set the flow state at the exit, one geometric parameter (the injection-exit area $A_3 = R\Delta\theta\Delta x$) representative of the injection length scale that set the injected mass flow, and one geometric parameter (the injection-exit aspect ratio $\Lambda = R\Delta\theta/\Delta x$) to have a first-order approximation of the injection shape. As claimed by Collin [55], literature lacks studies addressing the issue of the interaction of a jet and a shear layer, however, it is far more abundant concerning jets exiting from a flat plate into a transverse stream. According to this crossflow-jet literature [56], there is a blowing parameter relevant to the jet penetration. However, the choice of this parameter is varied to account for the flow complexity [56]: V_3/V_1 for uniform-density incompressible flows,

$$R_3 = \sqrt{(\rho_3 V_3^2/\rho_1 V_1^2)} \tag{2}$$

for heterogeneous subsonic or supersonic flows, and p_{i3}/p_{i1} (sometimes employed) for supersonic configurations. The effective velocity ratio R_3 was widely used to scale the crossflow-jet trajectory [57]. In the present cases, if both jet-flow states are chosen fully expanded at the ambient static pressure p_0, the values of this parameter are $R_3 = 1.16$, 1.49, and 1.81, respectively, for eight, four, and two injections (cases 4, 3, and 5), which is under the range of application of the trajectory correlations known by the authors [57]. However, this parameter stands for the initial momentum input $\rho_3 V_3^2$ and cannot represent the subsequent acceleration induced by an excessive exit static pressure p_3, as is the case for an underexpanded injection. This indicates that R_3 is not the most general significant parameter. This discrepancy is also noticed in recent studies [58,59]. Because a relevant physical notion is the force applied by the injection on the transverse flow, a unifying parameter may be the ratio of the relative dynalpy $D_3 = \rho_3 V_3^2 + p_3 - p_1$ of the injection over the crossflow dynalpy, where p_1 is a static pressure characteristic of the nonuniform incident crossflow [56,60,61]. Davis [9], who experimented with the influence of two transverse secondary injections in a primary jet, chose to scale an equivalent velocity ratio based on the latter quantity and then showed a good correlation between different injection regimes. For the discussion, we choose to use the dynalpy as a single measure of the injection force, even if the examination of former studies [62–64] focused on the supersonic crossflow-jet configuration may suggest the use of an additional parameter, such as the secondary-jet pressure ratio p_3/p_1, to describe the structure of underexpanded injections. To complete the parameter set of the mixing device made of equally distributed

identical radial injectors, N denotes the number of injections. We can then define a set of control parameters as $(p_{i3}, T_{i3}, M_3, A_3, \Lambda, N)$ and a set of global parameters as $(Q_3, D_3, M_3, A_3, \Lambda, N)$. Q_3 is the total mass flow to provide to the mixing device:

$$Q_3 = N \times \delta(\gamma, r)\frac{p_{i3}A_3}{\sqrt{T_{i3}}}\frac{1}{\Sigma(M_3)} \tag{3}$$

where $\delta(\gamma, r)$ is a function of γ and r, and $\Sigma(M_3)$ is the ratio of the exit section over the throat section of the injection. The dynalpy flux D_3 is the action means of each injector on the main jet flow:

$$D_3 = p_{i3}\left(1 + \gamma M_3^2\right)\left(1 + \frac{\gamma - 1}{2}M_3^2\right)^{-\frac{\gamma}{\gamma-1}} - p_1 \tag{4}$$

In the present study, all of the injectors tested are sonic; $M_3 = 1$; the total mass flow only depends on N, p_{i3}, T_{i3}, and A_3; and the dynalpy is entirely determined by p_{i3}, the momentum ratio R_3^2, and the secondary-jet pressure ratio p_3/p_1. In addition, the area of each injector is unchanged, and the total injection area $N \times A_3$ is only controlled by the number of injections N.

Effect of the Number of Injections

The effect of the number N of active injectors is discussed by the comparison of cases 3, 4, and 5 (see Table 1). Their core surface deformations are illustrated in Figs. 4 and 13. In the three cases, one can notice that injections have a strong action on the mean jet near field. The jet distortion induced by two and four active injectors is seen to extend far downstream, whereas the action of the eight-injector device seems to decrease quickly along the jet. This RANS result stems from the turbulent diffusion of longitudinal vortices: those of the two- and four-injector devices (see Fig. 5) are conserved further downstream than in the eight-injector configuration (not shown here). This behavior is visible in Figs. 12a and 12c. Considering the decrease of the mean total pressure in Fig. 12c, we can notice that the eight-injector configuration is comparable with both of the others up to approximately $x/D = 2$ and then gradually becomes inactive, because it tends to have the same evolution as the noncontrolled jet. This is even more striking when looking at the jet expansion in Fig. 12a: the equivalent jet diameter undergoes the same growth as the reference jet's. For both the two and four-injector systems, two expansion-growth regimes may be distinguished, first a rapid regime and then a slower regime, similar to a saturation phase. It is more pronounced in the four-injector case. In the light of global criteria gathered in Table 2, one can see that the two-injector case has a smaller core volume than the four-injector case, which is due to a deeper secondary-jet penetration. This may be explained by the fact that the two vortex doublets interact later than the four vortex doublets, which makes the penetration stage described in Fig. 5 longer. This assertion is confirmed by the computed values of the minimum radial positions of the vortices: $(R_G/D)_{\min} = 0.49$ and 0.32 for the four-injector device and the two-injector device, respectively. In the case of eight active injectors, the radial evolution of longitudinal vortices shows that the penetration stage does not even exist and that the vortices diverge from the very beginning of the jet. On the other hand, with regard to the jet volume and the mean p_i, the four-injector configuration seems to have a better diffusion capability of the total pressure, due to an extended jet area and a greater shape factor.

In Table 2, a conventional potential core length x_c/D is defined as the abscissa at which the stagnation pressure begins to drop, that is, the point at which the external mixing layer reaches the axis. Many studies [19,21] often estimate the efficiency of a mixing device by a survey of the stagnation pressure evolution on the jet axis (or that of a related quantity such as Pitot pressure, static pressure, Mach number or velocity). Nevertheless, this criterion is not appropriate to characterize the mixing enhancement of strongly distorted jet such as the two-injector case (top of Fig. 13). Indeed, as highlighted by earlier studies on tab-fitted nozzles [18,19], in this configuration, the primary jet is separated into two persistent parts of high energy (see
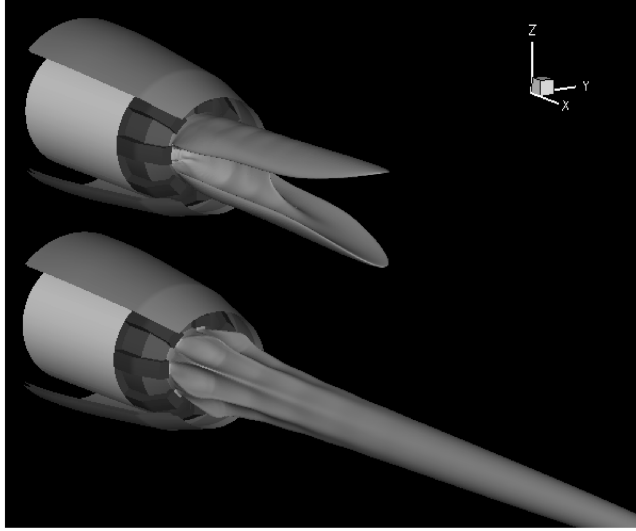
Fig. 13 Effect of two (top) and eight (bottom) radial injections on the core surface (iso-$p_i = p_{icore}$).

Fig. 14 Analogy of the force applied by a jet on a crossflow and the lift of an equivalent wing.

the two high-p_i lobes in Fig. 13), whereas the length x_c/D is dramatically reduced, compared with other cases (see Table 2).

In addition, Table 2 shows that even if the cross mass flows (ingoing and outgoing) are greater at the beginning of the two-injector-controlled jet (see Fig. 12c), the overall crossflows are larger in the four-injector case. This indicates that a distributed vortex doublet system transfers more crossflow than a system with concentrated vorticity patches, but that diffusion limits the actual number of vortices, as shown by the eight-injector case.

To sum up, the eight-injector device (case 4) is the least efficient, if not completely inefficient, the four-injector device (case 3) is the most powerful, and the two-injector device (case 5) does not behave very differently from the four-injector case. However, the thrust loss caused by the two-injector device (TL = 1.87%) is only 60% of the loss induced by the four-injector device (TL = 3.05%).

Influence of the Aspect Ratio of the Injections

Cases 3, 6, 7, and 8 allow us to investigate the influence of the aspect ratio $\Lambda = R\Delta\theta/\Delta x$ of the injector orifices, where Δx denotes the streamwise opening thickness and $R\Delta\theta$ is the spanwise dimension of each hole. All of the local and global criteria show that the lower the aspect ratio, the better the mixing is enhanced: faster and deeper penetration (Fig. 12b and core volume in Table 2), faster total pressure mixing (Fig. 12d and jet volume, mean p_i), and increased initial and total cross mass flows (Fig. 12f and Table 2).

To understand the effect of the injection aspect ratio on the hyper-mixing process, one must first know how it affects the penetration of each radial injection. For isolated crossflow jets, the CVP created by low-aspect-ratio injections was experimentally shown to penetrate deeper than the larger aspect ratios [53,65,66], even though some studies found an opposite trend, due to the axis-switching phenomenon [67]. To explain how the CVP properties are influenced by the injector aspect ratio, it is necessary to know how the CVP are generated. The latter issue is still not completely resolved, despite the advances brought by recent experimental [59,65,68–71] and numerical studies [72–75]. The general question is to know how the vorticity embedded in the skewed jet shear layer is oriented when it is convected downstream. The multitude of published scenarios probably reflects the diversity of the possible flow structures, depending, for instance, on the ejection velocity [59] or the orifice shape [65,71]. A further analysis is necessary, but is beyond the scope of this paper.

The law driving the evolution of the vorticity is included in the conservation of momentum, which is partially computed in RANS simulations in which the turbulent vortical scales are modeled. This explains why the CVP are reproduced by RANS computations [76] and why the influence of the aspect ratio was also captured by these
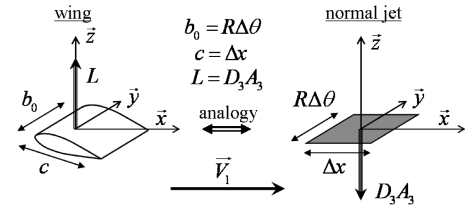
methods [77]. Nevertheless, RANS computations have difficulties in providing quantitative results, because of the turbulence modeling. To indicate how the input conditions may affect the subsequent CVP properties, let us consider the analogy between the force $D_3 A_3$ applied by each transverse injection on the primary-jet flow and the lift L created by a wing immersed in the same flow and for which chord and wingspan are, respectively, $c = \Delta x$ and $b_0 = R\Delta\theta$ (see Fig. 14). If Γ_0 is the maximum circulation around the equivalent wing, then we can assume that the circulation distribution reads $\Gamma(y) = \Gamma_0 \cdot f(y/b_0)$ with $f(0) = 1$ and $f(\pm 1/2) = 0$. Γ_0 is also the total circulation embedded in each of the two trailing vortices. If ρ_1 and V_1, respectively, denote the incident density and velocity on the equivalent wing, L then reads [78]

$$L = \rho_1 V_1 \int_{-b_0/2}^{+b_0/2} \Gamma(y)\, \mathrm{d}y = \rho_1 V_1 K \Gamma_0 b_0 \qquad (5)$$

where

$$K = \int_{-1/2}^{+1/2} f(\xi)\, \mathrm{d}\xi$$

$K = \pi/4$ for an elliptic lift distribution or, in other words, for a constant induced velocity on the equivalent wing. Making $D_3 A_3$ equal to L, we get a nondimensional expression of the trailing circulation:

$$\frac{\Gamma_0}{V_1 b_0} = \frac{1}{K} \frac{D_3}{\rho_1 V_1^2} \frac{1}{\Lambda} \qquad (6)$$

As the impulse introduced by the injector is conserved downstream, the spacing between the two trailing vortices further downstream is $b = K \cdot b_0$. Each vortex, considered as 2-D and concentrated at such location, induces a velocity $V_i = \Gamma_0/(2\pi b)$ on the other vortex of the doublet. The nondimensional penetration velocity of each doublet is then

$$\frac{V_i}{V_1} = \frac{1}{2\pi K^2} \frac{D_3}{\rho_1 V_1^2} \frac{1}{\Lambda} \qquad (7)$$

This expression indicates that reducing the aspect ratio of the injection orifice, while keeping all other parameters constant, will increase the penetration velocity and, hence, the velocity gradients. It is a qualitative model that ignores the intricate vortical dynamics of the jet-shear layer, thus, it should not be considered to quantify the far-field CVP.

A key component of the hyper-mixing process is the evolution of the streamwise vortices, characterized by a first stage in which initial CVPs converge toward the jet axis and a second stage in which new CVPs diverge (see Fig. 5). The first stage ends when all of the vortices are equally spaced in azimuth on a circle of minimum radius $(R_G/D)_{\min}$ [for example, case 3, depicted in Fig. 5 ($X/D = 3.0$)]. Thus, the vortices move closer to the jet axis if the initial vortex spacing is smaller (i.e., for small aspect-ratio injector orifices). This once again promotes the use of small aspect ratio injectors.

However, we can observe a saturation of the benefit to reduce the aspect ratio near a value of $\Lambda = 1$ (the curves drawn in Figs. 12b, 12d, and 12f). In this range of small aspect ratios, the dispersion radius of the vortices forming the CVP is probably large compared with their spacing, which explains the crucial role played by turbulent diffusion of the vorticity. Moreover, reducing the injector

aspect ratio decreases the space between the jet lobes (see Figs. 4 and 5) into which the external fluid can rush.

Influence of the Total Pressure of the Injections

A comparison of cases 2 and 3 illustrates the effect of a variation in the total pressure of the injection. As expected, all of the global criteria show that mixing is improved, together with the secondary-jet penetration, as the injection stagnation pressure p_{i3} is increased. The previously discussed variations were performed with a constant injection mass flow rate. From the four-injector case to the two-injector case, the mass flow distributed on each active injector is doubled by multiplying p_{i3} by a factor of 2. The 2-D inviscid vortex dynamics are solely dependent on the injector number N. In particular, it means that the minimum radius to the jet axis reached by the longitudinal vortices $(R_G/D)_{min}$ does not depend on p_{i3}. An increase in the stagnation pressure only scales the longitudinal evolution of the 2-D vortex system, namely, it accelerates the penetration of the initial doublets and advances the minimum radius $(R_G/D)_{min}$. Nevertheless, this rather simple reasoning does not account for the underexpanded secondary-jet near field in which the effect of the stagnation pressure p_{i3} was shown to determine the earlier jet penetration [62,79,80]. Moreover, in real flow, viscosity, turbulence, and instability may involve a different behavior. Concerning the thrust loss, it is all the more increased as the mixing efficiency is high.

Influence of the Temperature of the Injections

The influence of a variation in the injection temperature is tested through cases 3, 9, and 10, in which the total temperature T_{i3} varies from 300 to 1200 K. Because all of the other parameters were kept constant, the injection mass flow rate was successively divided by $\sqrt{2}$ and 2 with respect to the initial configuration (case 3). From a strict inviscid reasoning, the isentropic properties (p_i, T_i) are conserved on each streamline of the primary jet and the secondary jets. Because both the external static pressure p_0 and the stagnation pressures p_{i1} and p_{i3} are unchanged, the Mach number field is also unchanged. An increase in the injection temperature T_{i3} by a factor τ will only result in a rescaling of the secondary-stream velocities by a factor $\sqrt{\tau}$. Introducing the notion of turbulent friction and conductivity will probably change this ideal vision of the flow and will make things far more complex. Nonetheless, an improvement in the turbulent mechanical and thermal diffusion can be expected, because the velocity and temperature gradients are increased between the primary and the secondary jets. Yet, as displayed in Table 2, all of the mixing criteria based either on the stagnation pressure or on the cross mass flow rates are unchanged by the temperature modification. We can also notice that the higher the injection temperature, the lower the thrust loss. To sum up, an increase in the secondary-jet temperature, even if it does not produce the expected additional mixing enhancement, enables keeping the initial mixing capability (assessed on the jet total pressure) while reducing both the injected mass flow and the thrust loss.

In the light of the latter result, we can speculate on an original means of reducing the jet temperature by the use of a hot secondary flow, provided that the enhancement of the mixing with cold surrounding air is efficient enough to compensate the additional injected heat. This assumption is discussed in the next section.

Mixing Control of a Hot Jet

To evaluate the cooling capability of the four-injector device tested with a cold primary jet (case 3), the jet temperature was increased to 1100 K (case 11). This temperature growth shortens the potential core of the reference jet by 26%. This trend, indicating a faster mixing in the hot jet, agrees well with former studies [81,82]. Two temperatures were chosen for the injected fluid: $T_{i3} = 300$ K (case 12) and $T_{i3} = 1100$ K (case 13). In both cases, the mixing criteria were calculated (see Table 2). Considering the criteria based on the stagnation pressure and the cross mass flows, the efficiency of the mixing enhancement previously observed in the cold jet is also

obtained in the hot jet. In that view, no significant difference may be detected between the cold and the hot injections, as was stated for the cold jet. The ΔT criteria is now used to check the assumption formulated at the end of the previous section. For the cold injection case, $\Delta T = -1.8\% < 0$ shows a modest overall cooling of the primary jet. On the contrary, for the hot injection case, $\Delta T = +12.3\% > 0$ shows a significant increase of the integrated temperature criterion. The radiation emitted from such a simulated controlled jet could then be higher than that emitted by the reference jet, which is the opposite of what was originally hoped. Moreover, the injection total pressure being kept constant, the cold injected mass flow rate is $\sqrt{(1100/300)} \approx 1.9$ times higher than the hot injected mass flow rate. This makes the last conclusion rather pessimistic for the global infrared signature reduction, because it states that an overall thermal reduction may consume a large amount of cold injection fluid. However, this assertion should be considered with caution, because the RANS method may be unable to predict the thermal field, especially when the mixing layers are affected by strong compressibility effects. Moreover, the estimation of the radiative properties of such a flow is a very complex issue, notably depending on the respective concentrations and emissivities of the different species populating the exhaust gases [3], which is beyond the scope of this study. What can be asserted from the present work is that radial injections allow one to distort the hot part of the jet to control its aspect ratio and depth, which can be observed from particular view angles.

Conclusions

Experimental and numerical means were used to investigate the mixing enhancement of an underexpanded supersonic jet subjected to radial secondary injections. Measurements allowed us to confirm the efficiency of such a device. Several configurations were tested to assess the influence of the nozzle pressure ratio and the number of active injectors and their flow rate. RANS computations permitted us to understand the modification of the inside supersonic waves and indicated that they do not contribute to the mixing enhancement. As far as the mean flow is concerned, the mixing process taking place in a jet distorted by radial injections is strongly actuated by longitudinal vortices. The link between the injection conditions and the properties of the longitudinal vortices is left for future work.

Several mixing criteria were proposed and a parametric study was carried out. It gave some indications for designing an efficient mixing device: the injector number should be quite small, less than or equal to four, to prevent premature vortex interaction and excessive diffusion; a low-aspect-ratio orifice is preferred, although the benefit is not significant under a unity value; and the stagnation pressure should be as high as possible (with regard to other technological constraints). In addition, an increase in the injection temperature proved to exhibit the same mixing capability with respect to the stagnation pressure, while decreasing the injected flow. However, it seems to have a negative effect on the global temperature field, thus, this solution may not be appropriate for thermal signature alleviation.

Nonetheless, some discrepancies between present computations and measurements point out that improvements can be brought to the numerical method. Owing to the crucial role of the turbulence dynamics and to the geometric complexity, hybrid RANS/LES methods [83] such as ZDES [37] seem to be necessary to pursue the investigation and to analyze unsteady processes such as screech mixing [84,85]. Recent ZDES of this case were performed [86] and provided very satisfying results in this way. It is also worth mentioning that despite the inability of RANS computations to properly predict the jet far field, the parametric study was useful to provide some indications on the sensitivity of the jet mixing to various parameters at a reasonable computational cost. Indeed, provided that ZDES are only performed to get the time-averaged flowfield, the computational cost of a ZDES parametric study would be about 20 times as great as the RANS study. For instance, if one case computed by a RANS simulation takes 24 h of CPU time, the whole ZDES parametric study will take 6240 h of CPU time (i.e., about 9 months of CPU time). Finally, the methodology and the

proposed criteria can be applied to any jet flowfield data to assess the capabilities of a mixing device.

Acknowledgment

Thanks are expressed to Pascal Molton of the Fundamental and Experimental Aerodynamics Department, ONERA, for providing all of the experimental data.

References

[1] Varney, G. E., "Infrared Signature Measurement Techniques and Simulation Methods for Aircraft Survivability," 15th Joint Propulsion Conference, Las Vegas, NV, AIAA Paper 79-1186, June 1979.

[2] Mahulikar, S. P., Rao, G. A., Sane, S. K., and Marathe, A. G., "Aircraft Plume Infrared Signature in Nonafterburning Mode," *Journal of Thermophysics and Heat Transfer*, Vol. 19, No. 3, July–Sept. 2005.

[3] Rao, G. A., and Mahulikar, S. P., "Aircraft Powerplant and Plume Infrared Signature Modelling and Analysis," 43rd Aerospace Sciences Meeting and Exhibit, Reno, NV, AIAA Paper 2005-221, 2005.

[4] Papamoschou, D., and Roshko, A., "The Compressible Turbulent Shear Layer: An Experimental Study," *Journal of Fluid Mechanics*, Vol. 197, 1988, pp. 453–477.

[5] Elliot, G. S., and Samimy, M., "Compressibility Effects in Free Shear Layers," *Physics of Fluids*, Vol. 2, No. 7, 1990, pp. 1231–1240.

[6] Goebel, S. G., and Dutton, J. C., "Experimental Study of Compressible Turbulent Mixing Layers," *AIAA Journal*, Vol. 29, No. 4, 1991, pp. 538–546.

[7] Chuech, S. G., Lai, M. C., and Faeth, G. M., "Structure of Turbulent Sonic Under-Expanded Free Jets," *AIAA Journal*, Vol. 27, No. 5, May 1989, pp. 549–559.

[8] Gutmark, E. J., Schadow, K. C., and Yu, K. H., "Mixing Enhancement in Supersonic Free Shear Flows," *Annual Review of Fluid Mechanics*, Vol. 27, Jan. 1995, pp. 375–417.

[9] Davis, M. R., "Variable Control of Jet Decay," *AIAA Journal*, Vol. 20, No. 5, 1982, pp. 606–609.

[10] Denis, S., "Contrôle du Développement des Couches de Mélange Axisymétriques Subsoniques par Jets Impactant," Ph.D. Thesis, Univ. de Poitiers, Poiters, France, 2000.

[11] Collin, E., Barre, S., and Bonnet, J.-P., "Experimental Study of a Supersonic Jet-Mixing Layer Interaction," *Physics of Fluids*, Vol. 16, No. 3, 2004, pp. 765–778.

[12] Elliot, G. S., Samimy, M., and Arnette, S. A., "Study of Compressible Mixing Layers Using Filtered Rayleigh Scattering Based Visualizations," *AIAA Journal*, Vol. 30, No. 10, 1992, pp. 2567–2569.

[13] Clemens, N. T., and Mungal, M. G., "Two- and Three-Dimensional Effects in the Supersonic Mixing Layer," *AIAA Journal*, Vol. 30, No. 4, 1992, pp. 973–981.

[14] Belovich, V. M., Samimy, M., and Reeder, M. F., "Dual Stream Axisymmetric Mixing in the Presence of Axial Vorticity," *Journal of Propulsion and Power*, Vol. 12, No. 1, 1996, pp. 178–185.

[15] Hu, H., Saga, T., Kobayashi, T., and Taniguchi, N., "A Study on a Lobed Jet Mixing Flow by Using Stereoscopic Particle Image Velocimetry Technique," *Physics of Fluids*, Vol. 13, No. 11, 2001, pp. 3425–3441.

[16] Bridges, J., and Wernet, M. P., "Measurements of Separate Flow Nozzles with Mixing Enhancement Features," NASA TM-2002-211592, 2002.

[17] Alkislar, M. B., Krothapalli, A., Choutapalli, I., and Lourenco, L. M., "Structure of Supersonic Twin Jets," *AIAA Journal*, Vol. 43, No. 11, Nov. 2005, pp. 2309–2318.

[18] Bradbury, L. J. S., and Khadem, A. H., "The Distortion of a Jet by Tabs," *Journal of Fluid Mechanics*, Vol. 70, 1975, pp. 801–813.

[19] Samimy, M., Zaman, K. B. M. Q., and Reeder, M. F., "Effect of Tabs on the Flow and Noise Field of an Axisymmetric Jet," *AIAA Journal*, Vol. 31, No. 4, Apr. 1993, pp. 609–619.

[20] Zaman, K. B. M. Q., Reeder, M. F., and Samimy, M., "Control of an Axisymmetric Jet Using Vortex Generators," *Physics of Fluids*, Vol. 6, No. 2, Feb. 1994, pp. 778–793.

[21] Behrouzi, P., and McGuirk, J. J., "Effect of Tab Parameters on Near-Field Jet Plume Development," *Journal of Propulsion and Power*, Vol. 22, No. 3, May–June 2006, pp. 576–585.

[22] Arakeri, V. H., Krothapalli, A., Siddavaram, V., Alkislar, M. B., and Lourenco, L. M., "On the Use of Microjets to Suppress Turbulence in a Mach 0.9 Axisymmetric Jet," *Journal of Fluid Mechanics*, Vol. 490, 2003, pp. 75–98.

[23] Parekh, D. E., Kibens, V., Glezer, A., Wiltse, J. M., and Smith, D. M., "Innovative Jet Flow Control: Mixing Enhancement Experiments," AIAA Paper 96-0308, 1996.

[24] Freund, J. B., and Moin, P., "Jet Mixing Enhancement by High-Amplitude Fluidic Actuation," *AIAA Journal*, Vol. 38, No. 10, Oct. 2000, pp. 1863–1870.

[25] Chenault, C. F., Dorris, J., III, Smith, D., and Kibens, V., "Active Core Exhaust (ACE) Control for Reduction of Thermal Loading," AIAA Fluids 2000 Conference and Exhibit, Denver, CO, AIAA Paper 2000-2471, 2000.

[26] Ibrahim, M. K., Kunimura, R., and Nakamura, Y., "Mixing Enhancement of Compressible Jets by Using Unsteady Microjets as Actuators,". *AIAA Journal*, Vol. 40, No. 4, Apr. 2002, pp. 681–688.

[27] Delville, J., Collin, E., Lardeau, S., Lamballais, E., Barre, S., and Bonnet, J. P., "Control of Jets by Radial Fluid Injection," *ERCOFTAC Bulletin*, No. 44, pp. 57–67, 2000.

[28] Lardeau, S., Collin, E., Lamballais, E., and Bonnet, J.-P., "Analysis of a Jet-Mixing Layer Interaction," *International Journal of Heat and Fluid Flow*, Vol. 24, No. 2, 2003, pp. 520–528.

[29] Papamoschou, D., "Mixing Enhancement Using Axial Flow," AIAA Paper 2000-0093, 2000.

[30] Strykowski, P. J., Krothapalli, A., and Wishart, D., "Enhancement of Mixing in Highspeed Heated Jets Using a Counterflowing Nozzle," *AIAA Journal*, Vol. 31, No. 11, Nov. 1993, pp. 2033–2038.

[31] Molton, P., Jacquin, L., Chauvet, N., and Deck, S., "Mixing Enhancement in Under-Expanded Jet, Part 1," *Proceedings of the AAAF Symposium on Applied Aerodynamics* [CD-ROM], Paper 34_19_P, Association Aeronautique et Astronautique de France, Paris, 2006.

[32] Péchier, M., "Prévisions Numériques de L'Effet Magnus Pour des Configurations de Munition," Ph.D. Thesis, Department of Mechanical Engineering, Univ. de Poitiers, Poitiers, France, Sept. 1999.

[33] Péchier, M., Guillen, P., and Caysac, R., "Magnus Effect over Finned Projectiles," *Journal of Spacecraft and Rockets*, Vol. 38, No. 4, 2001, pp. 542–549.

[34] Deck, S., Duveau, P., d'Espiney, P., and Guillen, P., "Development and Application of Spalart Allmaras One Equation Turbulence Model to 3-D Supersonic Complex Configurations," *Aerospace Science and Technology*, Vol. 6, No. 3, 2002, pp. 171–183.

[35] Larchevêque, L., "Les of a Compressible Flow Past a Deep Cavity," *Physics of Fluids*, Vol. 15, No. 1, 2003, pp. 193–210.

[36] Deck, S., "Numerical Simulation of Transonique Buffet over a Supercritical Airfoil," *AIAA Journal*, Vol. 43, No. 7, July 2005, pp. 1556–1566.

[37] Deck, S., "Zonal Detached Eddy Simulation of the Flow Around a High-Lift Configuration," *AIAA Journal*, Vol. 43, No. 11, Nov. 2005, pp. 2372–2384.

[38] Simon, F., Deck, S., Guillen, P., and Sagaut, P., "Reynolds-Averaged Navier–Stokes/Large Eddy Simulations of Supersonic Base Flow," *AIAA Journal*, Vol. 44, No. 11, Nov. 2006.

[39] Dandois, J., Garnier, E., and Sagaut, P., "Unsteady Simulation of a Synthetic Jet in a Crossflow," *AIAA Journal*, Vol. 44, No. 2, Feb. 2006, pp. 225–238.

[40] Spalart, P. R., and Allmaras, S. R., "A One Equation Turbulence Model for Aerodynamics Flows," AIAA Paper 92-0439, 1992.

[41] Spalart, P. R., and Allmaras, S. R., "A One Equation Turbulence Model for Aerodynamics Flows," *La Recherche Aérospatiale*, Vol. 1, 1994, pp. 5–21.

[42] Georgiadis, N. J., Rumsey, C. L., Yoder, D. A., and, Zaman, M. Q. K. B., "Turbulence Modeling Effects on Calculation of Lobed Nozzle Flowfields," *Journal of Propulsion and Power*, Vol. 22, No. 3, May–June 2006, pp. 567–575.

[43] Payne, J. L., Roy, C. J., and Beresh, S. J., "A Comparison of Turbulence Models for a Supersonic Jet in Transonic Crossflow," 39th Aerospace Sciences Meeting and Exhibit, Reno, NV, AIAA 2001-1048, 2001.

[44] Dacles-Mariani, J., Zilliac, G. G., Chow, J. S., and Bradshaw, P., "Numerical-Experimental Study of a Wingtip Vortex in the Near Field," *AIAA Journal*, Vol. 33, No. 9, Sept. 1995, pp. 1561–1568.

[45] Kamotani, Y., and Greber, I., "Experiments on a Turbulent Jet in a Cross Flow," *AIAA Journal*, Vol. 10, No. 11, 1972, pp. 1425–1429.

[46] Fearn, R., and Weston, R. P., "Vorticity Associated with a Jet in a Cross Flow," *AIAA Journal*, Vol. 12, No. 12, Dec. 1974, pp. 1666–1671.

[47] Zaman, K. B. M. Q., "Axis Switching and Spreading of an Asymmetric Jet: The Role of Coherent Structure Dynamics," *Journal of Fluid Mechanics*, Vol. 316, 1996, pp. 1–27.

[48] Zaman, K. B. M. Q., "Spreading Characteristics of Compressible Jets from Nozzles of Various Geometries," *Journal of Fluid Mechanics*, Vol. 383, 1999, pp. 197–228.

[49] Chauvet, N., Deck, S., Jacquin, L., and Molton, P., "Experimental-Numerical Investigation of Mixing Enhancement in Under-Expanded Jet," Propulsion Conference and Exhibit, Sacramento, CA, AIAA

Paper 2006-4975, 2006.

[50] Love, E. S., and Grisby, C. E., "Some Studies of Axisymmetric Free Jets Exhausting from Sonic and Supersonic Nozzles into Still Air and into Supersonic Streams," NACA RM-L54L31, May 1955.

[51] Chauvet, N., Deck, S., and Jacquin, L., "Shock Patterns in a Slightly Under-Expanded Sonic Jet Controlled by Radial Injections," *Physics of Fluids* (to be published).

[52] Karagozian, A. R., "An Analytical Model for the Vorticity Associated with a Transverse Jet," *AIAA Journal*, Vol. 24, No. 3, 1986, pp. 429–436.

[53] Jacquin, L., "Phenomenological Description and Simplified Modelling of the Vortex Wake Issuing from a Jet in a Crossflow," *La Recherche Aérospatiale*, No. 2, 1994, pp. 117–133.

[54] Wang, C. R., "Application of a Turbulence Model for Jet and Cross Flow Interaction," Fluids 2000, Denver, CO, AIAA Paper 2000-2655, 2000.

[55] Collin, E., "Etude de L'Injection Radiale de Fluide dans une Couche de Mélange Annulaire Supersonique. Application ã l'Augmentation du Mélange," Ph.D. Thesis, Department of Mechanical Engineering, Univ. de Poitiers, Poitiers, France, 2001.

[56] Margason, R. J., "Fifty Years of Jet in Cross Flow Research," *Computational and Experimental Assessment of Jets in Cross Flow*, CP-534, AGARD, Neuilly sur Seine, France, 1993.

[57] Priere, C., and Gicquel, L. Y. M., "Experimental and Numerical Studies of Dilution Systems for Low-Emission Combustors," *AIAA Journal*, Vol. 43, No. 8, Aug. 2005, pp. 1753–1766.

[58] Muppidi, S., and Mahesh, K., "Study of Trajectories of Jets in Crossflow Using Direct Numerical Simulations," *Journal of Fluid Mechanics*, Vol. 530, 2005, pp. 81–100.

[59] Huang, R. F., and Lan, J., "Characteristic Modes and Evolution Processes of Shear-Layer Vortices in an Elevated Transverse Jet," *Physics of Fluids* [online journal], Vol. 17, No. 3, http://scitation.aip.org/dbt/dbt.jsp?KEY=PHFLE6&Volume=17.

[60] Schetz, J. A., and Billig, F. S., "Penetration of Gaseous Jets Injected into a Supersonic Stream," *Journal of Spacecraft*, Vol. 3, No. 11, 1966, pp. 1658–1665.

[61] Heister, S. D., and Karagozian, A. R., "Gaseous Jet in Supersonic Crossflow," *AIAA Journal*, Vol. 28, No. 5, May 1990, pp. 819–827.

[62] Zukovski, E. E., and Spaid, F. W., "Secondary Injection of Gases into a Supersonic Flow," *AIAA Journal*, Vol. 2, No. 10, 1964, pp. 1689–1688.

[63] Schetz, J. A., and Billig, F. S., "Structure of Highly Underexpanded Transverse Jets in a Supersonic Stream," *AIAA Journal*, Vol. 5, No. 5, 1966, pp. 882–884.

[64] Billig, F. S., Orth, R. C., and Lasky, M., "A Unified Analysis of Gaseous Jet Penetration," *AIAA Journal*, Vol. 9, No. 6, 1971, pp. 1048–1058.

[65] Haven, B. A., and Kurosaka, M., "Kidney and Anti-Kidney Vortices in Crossflow Jets," *Journal of Fluid Mechanics*, Vol. 352, 1997, pp. 27–64.

[66] Tomioka, S., Jacobsen, L. S., and Schetz, J. A., "Sonic Injection from Diamond-Shaped Orifices into a Supersonic Crossflow," *Journal of Propulsion and Power*, Vol. 19, No. 1, 2003, pp. 104–114.

[67] Gruber, M. R., and Nejad, A. S., "Transverse Injection from Circular and Elliptic Nozzles into a Supersonic Crossflow," *Journal of Propulsion and Power*, Vol. 16, No. 3, 2000, pp. 449–457.

[68] Fric, T. F., and Roshko, A., "Vortical Structure in the Wake of a Transverse Jet," *Journal of Fluid Mechanics*, Vol. 279, 1994, pp. 1–47.

[69] Kelso, R. M., Lim, T. T., and Perry, A. E., "An Experimental Study of Round Jets in Crossflow," *Journal of Fluid Mechanics*, Vol. 306, 1996, pp. 111–144.

[70] Lim, T. T., New, T. H., and Luo, S. C., "On the Development of Large-Scale Structures of a Jet Normal to a Cross Flow," *Physics of Fluids*, Vol. 13, No. 3, 2001, pp. 770–775.

[71] New, T. H., Lim, T. T., and Luo, S. C., "Elliptic Jets in Cross-Flow," *Journal of Fluid Mechanics*, Vol. 494, 2003, pp. 119–140.

[72] Yuan, L. L., Street, R. L., and Ferziger, J. H., "Large-Eddy Simulations of a Round Jet in Crossflow," *Journal of Fluid Mechanics*, Vol. 379, 1999, pp. 71–104.

[73] Cortelezzi, L., and Karagozian, A. R., "On the Formation of the Counter-Rotating Vortex Pair in Transverse Jets," *Journal of Fluid Mechanics*, Vol. 446, 2001, pp. 347–373.

[74] Marzouk, Y. M., and Ghoniem, A. F., "Mechanism of Streamwise Vorticity Formation in a Transverse Jet," 40th Aerospace Sciences Meeting and Exhibit, Reno, NV, AIAA Paper 2002-1063, 2002.

[75] Pinon, G., Bratec, H., Huberson, S., Pignot, G., and Rivoalen, E., "Vortex Method for Simulation of a 3-D Round Jet in a Cross-Stream," *Journal of Turbulence*, Vol. 6, No. 18, 2005, pp. 1–25.

[76] Sykes, R. I., Lewellen, W. S., and Parker, S. F., "On the Vorticity Dynamics of a Turbulent Jet in a Crossflow," *Journal of Fluid Mechanics*, Vol. 168, 1986, pp. 393–413.

[77] Foster, L. E., and Engblom, W. A., "Computation of Transverse Injection into Supersonic Crossflow with Various Injector Orifice Geometries," 42nd Aerospace Sciences Meeting and Exhibit, Reno, NV, AIAA Paper 2004-1199, 2004.

[78] Batchelor, G. K., *An Introduction to Fluid Dynamics*, 1st ed., Cambridge Univ. Press, New York, 1967.

[79] Cohen, L., Coulter, L. J., and Egan, W. J., Jr., "Penetration and Mixing of Multiple Gas Jets Subjected to a Cross Flow," *AIAA Journal*, Vol. 9, No. 4, pp. 718–724, 1971.

[80] Hermanson, J. C., and Winter, M., "Mie Scattering Imaging of a Transverse, Sonic Jet in Supersonic Flow," *AIAA Journal*, Vol. 31, No. 1, 1993, pp. 129–132.

[81] Lau, J. C., and Morris, P. J., "Effects of Exit Mach Number and Temperature on Mean-Flow and Turbulence Characteristics in Round Jets," *Journal of Fluid Mechanics*, Vol. 105, 1981, p. 193.

[82] Dash, S. M., Wolf, D. E., and Seiner, J. M., "Analysis of Turbulent Underexpanded Jets, Part 1: Parabolized Navier–Stokes Model SCIPVIS," *AIAA Journal*, Vol. 23, No. 4, April, 1984, pp. 505–514.

[83] Sagaut, P., Deck, S., and Terracol, M., *Multiscale and Multiresolution Approaches in Turbulence*, Imperial College Press, London, 2006.

[84] Krothapalli, A., Hsia, Y., Baganoff, D., and Karamcheti, K., "The Role of Screech Tones in Mixing of an Underexpanded Rectangular Jet," *Journal of Sound and Vibration*, Vol. 106, Apr. 1986, pp. 119–143.

[85] Rice, E. J., and Raman, G., "Enhancement Mixing of a Rectangular Supersonic Jet by Natural and Induced Screech," AIAA Paper 93-3263, 1993.

[86] Chauvet, N., Deck, S., and Jacquin, L., "Zonal Detached Eddy Simulation of a Controlled Propulsive Jet," *AIAA Journal* (submitted for publication).

P. Givi
Associate Editor